After Tropical Cyclones: Anticipating Environmental Element Changes within Estuarine Systems Using Spatio-Temporal Graph Neural Networks

Gaowei Zhang[1], **Jinrun Li**[1], **Wei Wang**[1], **Yi Wang**[1]

[1]Beijing University of Posts and Telecommunications
{zhangggaowei, lijinru, weiwang, yiwang}@bupt.edu.cn

Abstract

As the interfaces of land, ocean, and atmosphere ecosystems, estuarine systems have the unique importance in global ecosystems and economies for the rich and constant exchanges among multiple ecosystems. Tropical cyclones have the power to introduce drastic exchange of seawater and river water within estuaries, resulting in temporary fluctuations in salinity levels and other environmental parameters. Such fluctuations have profound effects on estuarine systems. Therefore, precisely predicting such fluctuations could contribute to informed decision-making and preparations for maintaining the resilience of estuarine systems when facing disastrous tropical cyclones. While graph-based deep learning models have made impressive achievements in environmental parameters predictions, they often have serious limitations for failing to explore complex dynamic inter-dependencies among different marine elements between various observation stations, thus restricting their applications in tasks related to estuarine systems. To this end, we introduce a feature representation based on energy-constrained diffusion synergizing with ocean dynamics to systematically integrates information from other observation points through their interactions. With the data collected from 24 observation points in the Yangtze River Estuary following three tropical cyclones, our extensive analyses show that our approach simulates the interplay and evolution of observation points, offering a comprehensive approach for comprehending dynamic changes within marine systems. Therefore, our approach provides effective predicting and interpreting the dynamics of environmental parameters in estuarine ecosystems following tropical cyclones, thus enabling robust support to various decision-making and participation tasks in protecting against the disturbances to estuarine systems resulting from tropical cyclones.

Introduction

Estuarine systems, as crucial interfaces connecting land, river, atmosphere, and ocean ecosystems, play an essential role in the global ecology and economy (Freeman et al. 2019). For example, Estuarine areas accounted for 40 percent of the population, 39 percent of employment, and 47 percent of economic output in the United States (NOAA 2022). The intricate interplay among wind, waves, and tidal forces, together with human activities, makes estuaries incredibly dynamic and sensitive (Cloern et al. 2016). Tropical cyclones, when passing estuaries, can generate large storm surge, strong waves, and subsequent river flooding, resulting in dramatic exchanges of seawater and river water within estuaries (Beudin et al. 2017). These exchanges can lead to a temporary fluctuations in salinity levels and other environmental parameters, which have profound impacts on the delicate balance of estuarine systems (Chu and Tan 2014). The global climate changes have caused the substantial increases in the frequency of the most intense cyclones (Knutson et al. 2010), thus put estuaries under pressure to make stronger responses to tropical cyclones in protecting estuarine ecosystems. Therefore, accurate predicting environmental disturbances holds paramount importance in facilitating informed decision-making and proactive preparations to bolster the resilience of estuarine ecosystems when confronting the devastating forces of tropical cyclones.

The environmental disturbances caused by the tropical cyclones' passage to estuaries are conventionally estimated with mathematical modeling techniques (Cuadra et al. 2014; Chen et al. 2015). While such techniques did help response teams in many protecting and recovering scenarios, they usually come with certain limitations, since they usually are simplifications of complex physical processes. Thus, the discrepancies between model predictions and real-world become inevitable. The intricate interplay of wind, waves and tides during tropical cyclone events presents a challenge for accurately representing all these complexities within a mathematical framework (Wang, Peng, and Liang 2022). Furthermore, feedback loops and dynamic interactions within storm surge events may not be adequately captured by traditional mathematical models, limiting their ability to simulate the intricate mechanisms driving surge development and propagation (Zhi et al. 2021).

The recent development of deep learning offers opportunities to address the shortcomings of conventional environmental disturbances prediction techniques. Among many deep learning models, graph-based deep learning models have the potential to significantly advance the status of post-storm environmental disturbances in estuaries(Adeli et al. 2023). While GNNs are promising in handling complex, nonlinear relationships within storm surge dynamics, they also suffer from substantial limitations in capturing the intricate and dynamic inter-dependencies that exist among various marine elements across spatially dispersed observation

stations. Furthermore, GNNs are sensitive to the initial structure of the graph, which requires a deep understanding of the underlying physical processes to get a promising results. This deficiency curtails their applicability in tasks pertaining to estuarine systems.

To address these challenges and realize the potential of GNNs, we present an innovative approach that harnesses a feature representation layer based on energy-constrained diffusion in tandem with ocean dynamics (Wu et al. 2023). As the key component of our model, the energy-based constraint module, inspired by an analogy with heat diffusion on a Riemannian manifold, is employed to determine how information flows over instances and the evolutionary direction of instance states. By seamlessly integrating information gleaned from multiple observation points through their intricate interactions, our approach yields a holistic comprehension of the complex interplay and evolution of these observation points.

We further compile a unique dataset from the observations of the aftermath of three distinct tropical cyclones recorded by six strategically-positioned observation points within the Yangtze River Estuary. Our extensive analyses with the data demonstrate that the approach adeptly simulate the nuanced interactions and evolutionary trajectories of observations from these observation points. Our approach does not only unravel the intricate dynamics among multiple forces but also establish an effective benchmark for forecasting and interpreting the fluctuating environmental parameters within estuarine ecosystems following the passage of tropical cyclones.

By enabling a robust comprehension of the dynamic changes that transpire within estuarine ecosystems, our model equips decision-makers and stakeholders with a practical tool to support diverse tasks aimed at safeguarding estuarine systems from the disruptive impacts inflicted by tropical cyclones. In essence, our innovative approach bridges the gap in predictive capabilities, which would eventually enhance the resilience of estuarine systems against the disruptive forces of tropical cyclones. By unraveling the intricate web of interactions, we pave the way for more effective strategies to mitigate and manage the impacts of storm surges within estuarine systems. Therefore, the contributions of our approach are tri-fold.

- **A novel learning representation** serves as an effective tool for encoding a batch of instances from estuarine ecosystems, featuring a Physics-inspired energy-based constraint module and a mechanism of dynamic adaptive generation of graphs.
- **A meticulously constructed dataset** contains environmental data of multiple distinct tropical cyclones from various observation stations in Yangtze River Estuary, which was developed with rigorous quality control measures to mitigate potential errors and inconsistencies.
- **A carefully-designed field evaluation** of the proposed model demonstrates the accuracy and capacity to foresee the intricate interplay of environmental factors, fostering more precise predictions.

Related Work

Traditional Numerical Methods. With the continuous advancement and refinement of mathematical modeling methods, storm surge models in estuarine regions have also been steadily progressing, such as the United States' SLOSH model (Forbes et al. 2014), the Netherlands' DELFT3D model (Symonds et al. 2016), and Denmark's MIKE model (Ma et al. 2016), have found widespread application in the study of estuarine storm surges. The SLOSH model, developed based on the first-generation storm surge numerical forecasting model SPLASH, has been improved to forecast typhoon-induced surges in coastal and lake areas, with its coverage extending over a significant portion of continental shelf waters and certain inland water bodies (Forbes et al. 2014). Particularly, it is extensively utilized for hurricane simulations along the U.S. West Coast. The DELFT3D model excels in multidimensional and non-steady flow simulations, holding a prominent position in storm surge simulations. Mendes et al. (2021) employed the flow module for storm surge simulation and accurately replicated the marine flooding during Typhoon Haiyan in the Bantayan area. The MIKE model, developed by the Danish Hydraulic Institute, is a comprehensive mathematical model used to study various elements such as hydrodynamics, temperature, salinity, and sediment in nearshore regions, and it enjoys widespread usage in estuarine areas (Ma et al. 2016).

Deep Learning Models. Deep learning has enabled novel solutions for oceanic spatio-temporal predictions. Ham, Kim, and Luo (2019) employed convolutional neural network (CNN) models for spatio-temporal prediction of the El Niño/Southern Oscillation phenomenon . This research demonstrated that the CNN model outperformed existing prediction methods in forecasting the Nino3.4 index with a forecast lead time extending up to a year and a half. Mulia et al. employed extreme learning machines for nearshore tsunami waveform prediction. Okuno, Aihara, and Hirata (2020) employed a suboptimal embedding framework to model all flood monitoring stations, enabling the long-term prediction of water levels in the target river section. These studies collectively highlight the efficacy of deep learning in enhancing the precision and lead time of oceanic spatio-temporal predictions, thereby contributing to a better understanding and management of various oceanic phenomena and potential hazards. Netto et al. (2022) developed a data-driven method to predict environmental variables such as current velocity and sea surface height in the region of Santos-Sao VicenteBertioga Estuarine System in the southeastern coast of Brazil.

Methodology

Overview of our Predictive Approach

We first introduce the general framework of our model's architecture. As shown in Figure 1, our model consits of three main components, which collectively form a comprehensive and integrated framework: (1) Feature representation layer; (2) Embedding layer; and (3) Graph learning layer. This holistic architecture synergistically integrate these components to provide a comprehensive understanding of the estu-

arine system. The feature representation layer is employed to ensure the incorporation of global information based on energy-constrained diffusion, while the adaptive embedding and graph learning layers enhance the model's ability to capture intricate details and complex dynamic relationships. These components enable our model to yield informed predictions and representations within estuarine ecosystems. We will detailed depicted the three components in the followings.

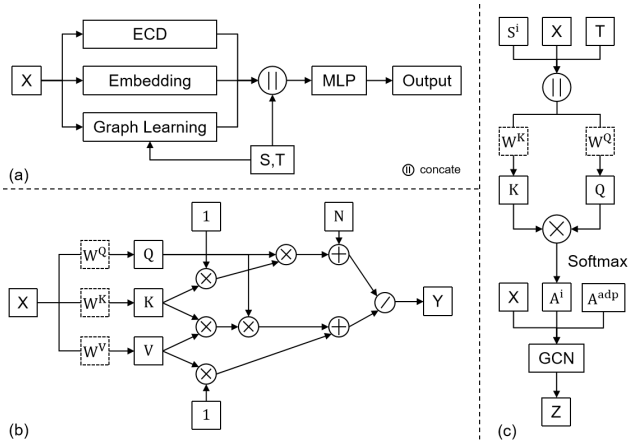

Figure 1: The overview of the proposed framework for forecasting within estuarine ecosystems: a) The overall framework of our model; b) Feature representation layer; and c) Graph learning layer.

Feature representation layer

In contrast to traditional methods that rely on fixed graph structures, the feature representation layer introduced in our model takes the collected entire estuary dataset (or a batch) of instances as input and encodes them into hidden states through an engergy-constrained diffusion process.

Following DIFFormer (Wu et al. 2023), the feature representation layer concept of our model stems from a diffusion process that treats a dataset of instances as a holistic entity, producing the representation through the intricate flow of information, which is inspired by the analogy to the diffusion of heat on a Riemannian manifold (Rosenberg 1997). Specifically, we employ a vector-valued function $y_i(t) : [0, \infty) \rightarrow R^d$ to define the state of an instance at a given time t and location i. This function captures the dynamic evolution of an instance's representation over time, reflecting both its inherent characteristics and its interactions within the broader context of the estuarine system. The anisotropic diffusion process in our model illustrate the intricate changes in instance states (i.e., representations) as they evolve.

Graph Learning Layer

In this section, we introduce a graph learning layer utilized in our framework. First, the fully connected layer undertakes the transformation of input time series data into latent space $X \in R^{N \times L}$. Subsequently, we concatenate spatial identities S^i, temporal identities T to X.

The spatial identities S^i takes into account the geographic relevance of the instances. Moreover, the temporal identities T in the chronological aspect, allowing the model to capture time-dependent variations and trends during each day. Following this, w_k and w_q are employed to calculate k and q, respectively. Ultimately, the product of k and q is utilized in conjunction with the $softmax$ function to derive the final adjacency matrix. The graph learning layer, through its incorporation of these diverse elements, serves as a dynamic substrate for information propagation and interaction. By encapsulating spatial, temporal, and target-related attributes, it facilitates a more comprehensive exploration of interdependencies, ultimately leading to enhanced predictive capabilities and deeper insights within our feature representation layer.

$$\begin{aligned} H^1 &= Concat[X, S^1, T^D] \\ H^2 &= Concat[X, S^2, T^D] \end{aligned} \tag{1}$$

$$\begin{aligned} A^1 &= Softmax(\frac{(H^1 W^Q)(H^1 W^K)^T}{\sqrt{d}}) \\ A^2 &= Softmax(\frac{(H^2 W^Q)(H^2 W^K)^T}{\sqrt{d}}) \end{aligned} \tag{2}$$

$$Z = A^1 X W^1 + A^2 X W^2 + A^{adp} X W^3 \tag{3}$$

where $A^{adp} = Softmax(ReLU(S^1(S^2)^T))$ denotes the self attention of spatial identities. X is the input time series. Z is the output of graph learning layer.

Graph Embedding Layer

The graph embedding layer of our mdoel is employed to capture the inherent relationships among instances within the collected estuarine system. The process involves mapping instances from their original feature space into a high-dimensional latent space. In this research, we first randomly initialize a node embedding dictionary $M_s \in R^{N \times d}$ with learnable parameters, where d denotes the dimension of node embedding. Then, we develop a self-adaptive adjacency matrix A_s which is named adjacency matrix to derive the long-term spatial dependency weights among the observation stations. The formula is as follows:

$$A_s = \mathrm{SoftMax}(\mathrm{ReLU}(M_s \cdot M_s^\top)) \tag{4}$$

During the training process, M_s will automatically update and learn the long-term representation vectors of different observation stations and get the adjacency matrix A_s according to Equation (4).

This graph embedding serves as a bridge between the intricate graph topology and the learning algorithms, enabling the model to effectively exploit the graph's dynamic structural properties. By projecting instances into a continuous vector space, the model can capture both local and global patterns, as well as interactions and dependencies that are important for making informed forecasting.

Experiments

The Yangtze River Delta (see Figure 2(a)) is situated on the East China Sea shelf, characterized by a vast maritime area and a high frequency of typhoon-induced storm surges. In addition, the Yangtze River Delta is an economically developed region with a dense population. In the event of a strong typhoon impact, coastal cities, particularly Shanghai and Hangzhou, could face significant losses in terms of both human lives and property.

This study focuses on the typhoons that cross or land in the Yangtze River Estuary region. To be more specific, we selected Typhoon Fung-wong (Typhoon No. 16 of 2014), Typhoon Ampil (Typhoon No. 10 of 2018), and Typhoon Lekima (Typhoon No. 9 of 2019) as the primary research contexts. Figure 2(c) depicts the detailed paths of these three typical typhoons. The distribution encompasses all 24 points, where 0, 1, 2, 3, 4, and 5 correspond to the six previously mentioned observation points. Points 6 through 23 represent additional observation points during the passage of the typhoon. These 24 points are divided into three routes, each consisting of eight points (see Figure 2(c)). Code and data used in evaluations are available at: https://figshare.com/articles/dataset/articles/23967366.

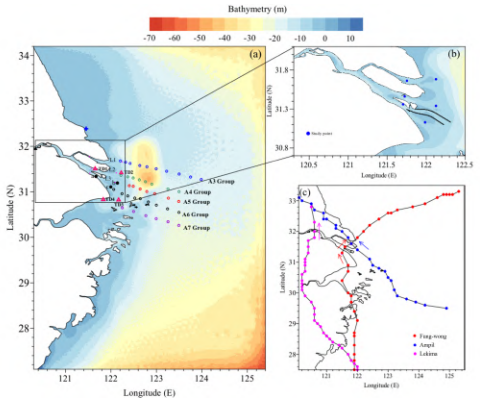

Figure 2: Overall study areas and paths of Typhoons.

Datasets

Fung-wong made landfall as a tropical storm on September 19, 2014, approximately 395 kilometers in the northwestern Pacific Ocean. On September 23, Fung-wong passed through the downstream of the northern branch of the Yangtze River Estuary (see the red-line in Figure 2(c)).

Ampil originated in the northwestern Pacific Ocean on July 20, 2018. On July 22, Ampil made landfall as a strong typhoon near Shanghai. It was the strongest typhoon to directly hit Shanghai since 1990, which holds a significant importance for the study of storm surge disasters in the Yangtze River Estuary (see the blue-line in Figure 2(c)).

Lekima originated in the northwestern Pacific Ocean on August 4, 2019. It made landfall in Zhejiang Province and passed through the upstream channel of the Yangtze River Estuary, as an extremely powerful super typhoon with a central wind force exceeding 17 on the Beaufort scale (see the purple-line in Figure 2(c)).

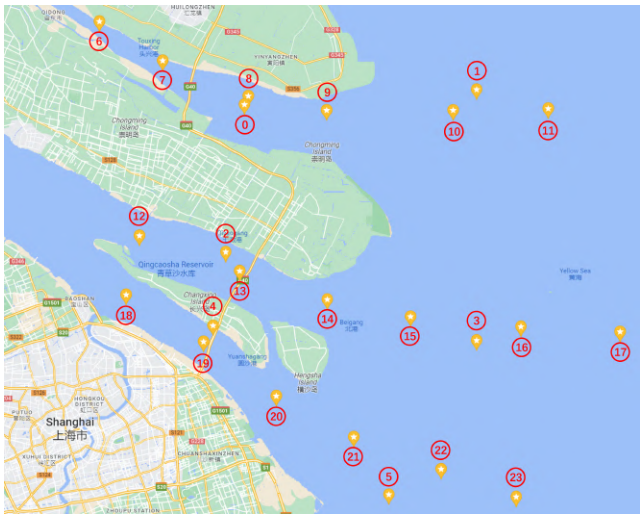

Figure 3: The distribution of 24 observation points during Typhoons in the Yangtze River Estuary region.

Each typhoon dataset consists of records from 24 observation points (see the observation stations 1-24 in Figure 3), with data being collected on a 5-minutes basis. Each data contains both water flow velocity and salinity levels. Fung-wong was monitored every 5 minutes from September 17th, 00:00, until October 1st, 00:00, resulting in a dataset of 4044 data points. Ampil underwent sampling at 5-minute intervals from July 15th at 00:00 to August 10th at 00:00, generating a dataset with 7500 data points. Typhoon Lekima (2019) was monitored every 5 minutes, spanning from August 3rd at 00:00 to August 20th at 00:00, yielding a dataset of 4908 data points. These datasets provide an detailed illustration of the behavior of these typhoons, capturing rapid changes in water flow velocity and salinity levels across multiple observation points. The high-frequency sampling enables a meticulous analysis of how these environmental factors evolved over the entire duration of each typhoon. In our experiments, 70% of the data is used for traning, while 20% and 10% are for validation and testing.

Ablation Study

We conduct an ablation study on Lekima to validate the effectiveness of key components of our model. The test results are shown in Table 1. We also incorporated curriculum learning into our model. The provided table presents a comprehensive comparison of performance metrics for various approaches in predicting two distinct variables: Velocity and Salinity. The evaluation metrics utilized include Mean Absolute Error (MAE), Root Mean Square Error (RMSE), and Mean Absolute Percentage Error (MAPE).

For the variable Velocity, the following approaches are assessed:

- w/o cl - This signifies the predictive approach without employing curriculum learning.
- w/o gl - Denoting our methodology without the incorpo-

Table 1: Ablation study on the Lekima dataset.

Data	Variant	MAE	RMSE	MAPE(%)
Velocity	w/o cl	0.0677	0.0915	0.1764
	w/o gl	0.0585	**0.0803**	**0.1594**
	w/o fr	0.0655	0.0893	0.1727
	ours	**0.0580**	0.0807	0.1610
Salinity	w/o cl	0.7891	1.2005	**0.3566**
	w/o gl	0.8088	1.2422	0.5701
	w/o fr	0.7640	1.1873	0.4138
	ours	**0.7599**	**1.1759**	0.3701

ration of graph learning.

- w/o fr - Represents our approach without incorporating feature representation layer.
- ours - Refers to our proposed predictive approach.

Similarly, for the variable Salinity, the same set of approaches are evaluated and compared.

Clearly, we can draw some key observations from Table 1. For velocity predictions, our approach outperforms other methods and demonstrates the most promising results across all three evaluation metrics (MAE, RMSE, and MAPE), suggesting superior predictive accuracy for the Velocity variable. In addition, among the other methods, our method without graph learning layer also exhibits competitive performance. Furthermore, it's worth noting that even when we exclude the graph learning layer from our approach, it can also exhibits competitive performance. This observation underscores the potential advantages of incorporating feature representation layer over the graph learning layer in velocity predictions.

For salinity predictions, our approach consistently outperforms the alternatives in terms of MAE, RMSE, and MAPE. It achieves the lowest values for these metrics, demonstrating its strong predictive capabilities for the Salinity variable. Notably, in contrast to velocity predictions, our approach without feature representation layer delivers competitive results, suggesting that graph learning holds greater importance than the feature representation layer in the Salinity prediction..

In conclusion, Table 1 outcomes highlight the effectiveness of our proposed approach in predicting both Velocity and Salinity. Its consistently superior performance across various evaluation metrics reaffirms its potential for accurate and reliable predictions in this context. Moreover, it underscores the significance of graph learning and feature representation layers in enhancing predictive accuracy for velocity and salinity, as demonstrated by the performance of w/o gl and w/o df.

Comparison with Other Methods

In this section, we conducted comparative experiments with other gnn-based methods. The detailed descriptions of these approaches are in below:

- LSTM (Hochreiter and Schmidhuber 1997): LSTM is a powerful recurrent neural network architecture designed to capture long-range dependencies in time series data, which is widely used for time series prediction.
- Graph WaveNet (Wu et al. 2019): Graph WaveNet incorporates graph convolution and dilated causal convolution to effectively capture spatial-temporal dependencies in data.
- MTGNN (Wu et al. 2020): MTGNN introduces a graph-learning module to establish relationships between variables. It connects hub nodes with their top k nearest neighbors in a metric space. The backbone architecture for temporal modeling is based on the WaveNet structure.
- AGCRN (Bai et al. 2020): AGCRN includes a graph-learning module to model inter-variable relationships. It employs personalized RNNs to capture temporal dependencies for each time series. The integration of GRU with graph convolutions adapts node parameters.
- STID (Shao et al. 2022a): STID is a simple yet effective baseline for MTS forecasting by attaching spatial and temporal identity information. STID achieves better efficiency and performance simultaneously based on simple networks.
- D2STGNN (Shao et al. 2022b): D2STGNN introduces a Decoupled Spatial-Temporal Framework (DSTF) that separates diffusion and inherent traffic information in data. It leverages graph neural networks to capture spatial dependencies.
- Crossformer (Zhang and Yan 2023): Crossformer is a transformer-based model designed for multivariate time series forecasting. It incorporates cross-dimensional dependencies to improve forecasting accuracy.

The comparison results are shown in Table 2. The table provides a comparison of performance metrics for different approaches in predicting two variables: Velocity and Salinity. The metrics measured are Mean Absolute Error (MAE), Root Mean Square Error (RMSE), and Mean Absolute Percentage Error (MAPE).

Table 2 provides a detailed comparison of experimental results with various predictive models across three distinct Typhoons in the Yangtze River Estuary: Fung-wong, Ampil, and Lekima. The evaluation metrics employed encompass Mean Absolute Error (MAE), Root Mean Square Error (RMSE), and Mean Absolute Percentage Error (MAPE).

For Velocity Predictions:

- Fung-wong: Among the evaluated models, our approach emerges as a standout performer, yielding the most compelling results in terms of MAE, RMSE, and MAPE metrics for velocity predictions. This underscores its robust predictive capability in capturing the intricate dynamics of the Fung-wong's velocity patterns.
- Ampil: Consistently, ours model attains superior outcomes, showcasing the lowest MAE, RMSE, and MAPE values. This signifies the model's adeptness in elucidating the complex velocity behaviors characteristic of the Ampil.
- Lekima: Our methodology once again outperforms the alternative models, presenting the lowest MAE, RMSE,

and competitive MAPE values. This underscores its aptitude in capturing the nuanced velocity fluctuations exhibited during the Lekima.

For Salinity Predictions:

- Fung-wong: Our model maintains its competitive advantage, yielding lower MAE, RMSE, and MAPE values for salinity predictions. This reflects its prowess in characterizing salinity variations during the Fung-wong.
- Ampil: Our approach continues to demonstrate superior performance, presenting superior results with lower MAE, RMSE, and MAPE metrics for salinity predictions. This underlines the model's effectiveness in delineating salinity dynamics during the Ampil.
- Lekima: Our model's performance clearly evident, achieving the lowest MAE and RMSE values, while maintaining a competitive MAPE score. This underscores its adeptness in capturing the intricate salinity variations associated with the Lekima.

In conclusion, the analysis of tabular data substantiates the efficacy of our predictive model across diverse meteorological events. Its consistent advantages across the MAE, RMSE, and MAPE metrics for both velocity and salinity predictions underscores its capacity to discern and predict intricate spatiotemporal patterns. This empirical validation lends credence to its potential as an advanced tool for enhancing meteorological predictions, warranting further exploration and consideration within the academic and scientific community.

Understanding Our Model's Effect with the MIKE Method

To better understand our model's effect, we utilize the outputs from our model's 24 observations and apply the MIKE method to calculate the flow velocity and salinity during the passage of Typhoon Fung-wong through the Yangtze River Estuary.

Figure 4 shows the generated current distribution before and after the passage of Fung-wong. Specifically, during the passage of Fung-wong, its intense atmospheric disturbances over the sea surface have a significant impact on water currents and waves. The variation in water current velocity during Fung-wong is illustrated in Figure 4 (a). At 6:00 AM on September 22nd (Figure 4 (a)), when the typhoon initially made landfall, the influence of the powerful cyclone led to turbulent changes in the water current directions at the northern branch of the Yangtze River mouth, as well as at the entrances of Nangang and Beigang harbors. As the typhoon followed its path across the southern and northern branches of the Yangtze River mouth, the flow velocity outside the mouth increased, with the ebb current stronger than the flood current. Furthermore, as Fung-wong made landfall at the Yangtze River mouth, it had weakened to the level of a tropical storm, exhibiting comparatively lower wind speeds than other strong typhoons. Consequently, its impact on sea currents was relatively minor, yet it still disrupted the flow directions at the mouth of the river. The landfall of Fung-wong coincided with a spring tide, amplifying the combined effects of strong winds and astronomical tides. Figure 4 also indicates that in the southern branch of the Yangtze River mouth, the ebb current is stronger than the flood current.

Figure 5 illustrates the salinity distribution changes during Fung-wong. To better understand the reasons behind these salinity distribution changes, the corresponding current distribution at each moment was included. Following Fung-wong's landfall, the salinity contour at 8 psu (practical salinity unit) shifted upwards due to the intense cyclonic disturbance on the sea surface and the effects of strong waves. This upward shift lead in potential risk to the safety of drinking water within the Yangtze River Estuary. After the typhoon passed, the 8 psu salinity contour shifted back, but due to the asymmetry of the tides with rising tide flows stronger than ebb tide flows and the specific topography, the inflow of high salinity water brought by the rising tide accumulated in the shallow waters near the estuary mouth. The ebb tide flow was insufficient to rapidly flush out the incoming high-salinity water, resulting in a prolonged period of elevated salinity levels at the estuary mouth. As the typhoon gradually moved away, the northern branch of the estuary remained enveloped in relatively high salinity levels. This phenomenon is attributed to the unique geographical features of the northern branch and the asymmetry of the tidal currents, highlighting the rapid response of salinity to the typhoon process, but indicating a slow recovery process. Furthermore, figure 5 illustrates the distribution of surface and bottom layer salinity before and after Fung-wong. Prior to the typhoon's landfall, the 30 psu salinity contour exhibited a larger and closer-to-the-mouth extent in the bottom layer. In conjunction with the current distribution, noticeable disparities in the magnitude and direction of flow velocities between surface and bottom layers are evident, contributing to the generation of longitudinal circulation. After the typhoon's landfall, the contours of equal salinity for surface and bottom layers nearly coincided, suggesting a uniform pattern in the longitudinal distribution influenced by the typhoon. Although surface flow velocities remained slightly greater, no distinct circulation was generated.

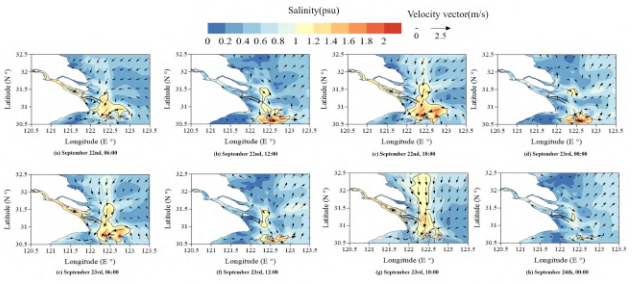

Figure 4: Current distribution before and after the passage of Fung-wong.

Conclusion

Estuarine systems are critical to the global ecology and economy but sensitive to extreme climate events such as tropical cyclones. To effectively protect Estuarine systems

Table 2: Performance comparison of different approaches on the Fung-wong, Ampil, and Lekima. Bold indicates the best results, underline indicates the second-best results.

Data		Metric	LSTM	GWNet	MTGNN	AGCRN	STNorm	STID	D2STGNN	Crossformer	ours
Fung-wong	Velocity	MAE	0.1293	0.1188	0.1110	0.1294	0.1245	0.1139	0.1166	0.1090	**0.1054**
		RMSE	0.1705	0.1556	0.1448	0.1730	0.1604	0.1475	0.1557	0.1443	**0.1388**
		MAPE(%)	0.4609	0.3540	0.3268	0.4451	0.3686	0.3446	0.3328	0.3835	**0.2966**
	Salinity	MAE	1.6672	1.2933	1.2403	2.9288	1.9989	1.3144	1.7046	1.1750	**1.1353**
		RMSE	2.5541	1.9472	1.7449	4.3512	2.9096	1.8306	2.4432	**1.6759**	1.9392
		MAPE(%)	88.823	27.947	31.687	29.313	27.624	35.548	**16.579**	53.982	30.150
Ampil	Velocity	MAE	0.0927	0.0609	0.0580	0.0534	0.0627	0.0650	0.0553	0.0633	**0.0533**
		RMSE	0.1227	0.0803	0.0795	**0.0716**	0.0854	0.0873	0.0739	0.0844	0.0744
		MAPE(%)	0.3461	0.2004	0.1853	**0.1607**	0.2159	0.2105	0.1734	0.2119	0.1635
	Salinity	MAE	0.8032	0.6228	0.5924	0.9279	0.7303	0.5848	0.6302	0.6639	**0.5667**
		RMSE	1.2873	1.1156	1.0509	1.6347	1.2495	1.0407	1.1321	1.1660	**1.0173**
		MAPE(%)	71.351	8.0823	12.656	19.564	17.654	8.9540	**4.6230**	30.626	16.043
Lekima	Velocity	MAE	0.1158	0.0787	0.0663	0.0603	0.0799	0.0677	0.0732	0.0775	**0.0580**
		RMSE	0.1528	0.1070	0.0894	0.0865	0.1115	0.0915	0.1017	0.1062	**0.0807**
		MAPE(%)	0.3117	0.2088	0.1754	**0.1565**	0.2144	0.1764	0.1765	0.2025	0.1610
	Salinity	MAE	1.7293	0.9714	0.8386	1.7022	1.3561	0.8033	1.0051	1.2317	**0.7599**
		RMSE	2.4954	1.5125	1.2284	2.7461	2.1604	1.2815	1.6113	1.8060	**1.1759**
		MAPE(%)	1.5500	1.0841	1.0728	0.8125	1.0128	0.5401	0.7940	0.8863	**0.3701**

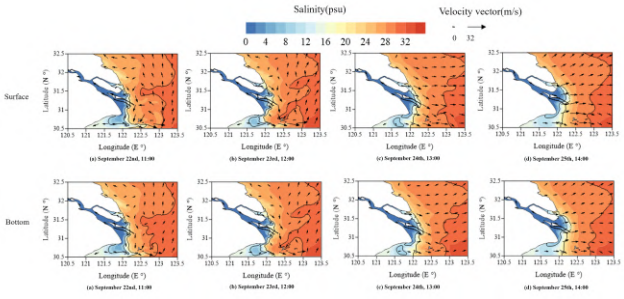

Figure 5: Salinity distribution of surface and bottom layer before and after the passage of Fung-wong.

against these events, precisely predicting environmental disturbances caused by them is of significant importance in maintaining estuarine systems' resilience. This paper proposes a novel learning representation featuring a Physics-inspired energy-based constraint module and a mechanism of dynamic adaptive generation of graphs. We evaluate it with a careful compiled dataset of multiple distinct tropical cyclones from various observation stations in Yangtze River Estuary. Our experimental results demonstrated the method can provide state-of-the-art predictions on multiple environmental paramenters after tropical cyclone pass estuaries. Moreover, it can be utilized to enhance the comprehension of the complex processes of the environmental disturbances resulting from intricate interplays between meteorological forces and hydrodynamic responses. Thus, our method delivers practical values in safeguarding estuarine systems from the disruptive impacts inflicted by tropical cyclones. As future research continues to delve into the intricate details of these interactions, we can better predict, manage, and mitigate the impact of super typhoons on estuarine environments, fostering a more resilient system of nature and human communities. Currently, we are working with the related oceanic administration agencies to deploy our method and will continue improve it in a real-world deployment.

Acknowledgements

This work is partially supported by National Natural Science Foundation of China under grants 62076232 and 62172049. Corresponding author: Wei Wang.

References

Adeli, E.; Sun, L.; Wang, J.; and Taflanidis, A. A. 2023. An advanced spatio-temporal convolutional recurrent neural network for storm surge predictions. *Neural Computing and Applications*, 1–17.

Bai, L.; Yao, L.; Li, C.; Wang, X.; and Wang, C. 2020. Adaptive Graph Convolutional Recurrent Network for Traffic Forecasting. In Larochelle, H.; Ranzato, M.; Hadsell, R.; Balcan, M.; and Lin, H., eds., *NeurIPS 2020, December 6-12, 2020, virtual*.

Beudin, A.; Ganju, N. K.; Defne, Z.; and Aretxabaleta, A. 2017. Physical response of a back-barrier estuary to a post-tropical cyclone. *Journal of Geophysical Research: Oceans*, 122(7): 5888–5904.

Chen, J.-L.; Hsu, T.-J.; Shi, F.; Raubenheimer, B.; and Elgar, S. 2015. Hydrodynamic and sediment transport modeling of N ew R iver I nlet (NC) under the interaction of tides and waves. *Journal of Geophysical Research: Oceans*, 120(6): 4028–4047.

Chu, K.; and Tan, Z.-M. 2014. Annular typhoons in the western North Pacific. *Weather and forecasting*, 29(2): 241–251.

Cloern, J. E.; Abreu, P. C.; Carstensen, J.; Chauvaud, L.; Elmgren, R.; Grall, J.; Greening, H.; Johansson, J. O. R.;

Kahru, M.; Sherwood, E. T.; et al. 2016. Human activities and climate variability drive fast-paced change across the world's estuarine–coastal ecosystems. *Global change biology*, 22(2): 513–529.

Cuadra, C.; Suarez, J. K.; Biton, N. I.; Cabacaba, K. M.; Lapidez, J. P.; Santiago, J.; Mahar Francisco Lagmay, A.; and Malano, V. 2014. Development of Inundation Map for Bantayan Island, Cebu Using Delft3D-Flow Storm Surge Simulations of Typhoon Haiyan. In *EGU General Assembly Conference Abstracts*, 15687.

Forbes, C.; Rhome, J.; Mattocks, C.; and Taylor, A. 2014. Predicting the storm surge threat of Hurricane Sandy with the National Weather Service SLOSH model. *Journal of Marine Science and Engineering*, 2(2): 437–476.

Freeman, L. A.; Corbett, D. R.; Fitzgerald, A. M.; Lemley, D. A.; Quigg, A.; and Steppe, C. N. 2019. Impacts of urbanization and development on estuarine ecosystems and water quality. *Estuaries and Coasts*, 42: 1821–1838.

Ham, Y.-G.; Kim, J.-H.; and Luo, J.-J. 2019. Deep learning for multi-year ENSO forecasts. *Nature*, 573(7775): 568–572.

Hochreiter, S.; and Schmidhuber, J. 1997. Long short-term memory. *Neural computation*, 9(8): 1735–1780.

Knutson, T. R.; McBride, J. L.; Chan, J.; Emanuel, K.; Holland, G.; Landsea, C.; Held, I.; Kossin, J. P.; Srivastava, A.; and Sugi, M. 2010. Tropical cyclones and climate change. *Nature geoscience*, 3(3): 157–163.

Ma, L.; He, C.; Bian, H.; and Sheng, L. 2016. MIKE SHE modeling of ecohydrological processes: Merits, applications, and challenges. *Ecological Engineering*, 96: 137–149.

Mendes, J.; Ruela, R.; Picado, A.; Pinheiro, J. P.; Ribeiro, A. S.; Pereira, H.; and Dias, J. M. 2021. Modeling dynamic processes of Mondego estuary and Óbidos lagoon using delft3D. *Journal of Marine Science and Engineering*, 9(1): 91.

Netto, C. F.; de Barros, M. R.; Coelho, J. F.; de Freitas, L. P.; Moreno, F. M.; Mathias, M. S.; Dottori, M.; Cozman, F. G.; Costa, A. H.; Gomi, E. S.; et al. 2022. Modeling Oceanic Variables with Dynamic Graph Neural Networks. *arXiv preprint arXiv:2206.12746*.

NOAA. 2022. Estuary Habitat. https://www.fisheries.noaa.gov/national/habitat-conservation/estuary-habitat. Accessed: 2023-08-06.

Okuno, S.; Aihara, K.; and Hirata, Y. 2020. Forecasting high-dimensional dynamics exploiting suboptimal embeddings. *Scientific Reports*, 10(1): 664.

Rosenberg, S. 1997. *The Laplacian on a Riemannian manifold: an introduction to analysis on manifolds*. 31. Cambridge University Press.

Shao, Z.; Zhang, Z.; Wang, F.; Wei, W.; and Xu, Y. 2022a. Spatial-Temporal Identity: A Simple yet Effective Baseline for Multivariate Time Series Forecasting. In Hasan, M. A.; and Xiong, L., eds., *CIKM 2022, Atlanta, GA, USA, October 17-21, 2022*, 4454–4458. ACM.

Shao, Z.; Zhang, Z.; Wei, W.; Wang, F.; Xu, Y.; Cao, X.; and Jensen, C. S. 2022b. Decoupled Dynamic Spatial-Temporal Graph Neural Network for Traffic Forecasting. *Proc. VLDB Endow.*, 15(11): 2733–2746.

Symonds, A. M.; Vijverberg, T.; Post, S.; Van Der Spek, B.-J.; Henrotte, J.; and Sokolewicz, M. 2016. Comparison between Mike 21 FM, Delft3D and Delft3D FM flow models of western port bay, Australia. *Coast. Eng*, 2: 1–12.

Wang, S.; Peng, H.; and Liang, S. 2022. Prediction of estuarine water quality using interpretable machine learning approach. *Journal of Hydrology*, 605: 127320.

Wu, Q.; Yang, C.; Zhao, W.; He, Y.; Wipf, D.; and Yan, J. 2023. DIFFormer: Scalable (Graph) Transformers Induced by Energy Constrained Diffusion. In *ICLR 2023, Kigali, Rwanda, May 1-5, 2023*. OpenReview.net.

Wu, Z.; Pan, S.; Long, G.; Jiang, J.; Chang, X.; and Zhang, C. 2020. Connecting the Dots: Multivariate Time Series Forecasting with Graph Neural Networks. In Gupta, R.; Liu, Y.; Tang, J.; and Prakash, B. A., eds., *KDD '20, Virtual Event, CA, USA, August 23-27, 2020*, 753–763. ACM.

Wu, Z.; Pan, S.; Long, G.; Jiang, J.; and Zhang, C. 2019. Graph WaveNet for Deep Spatial-Temporal Graph Modeling. In Kraus, S., ed., *IJCAI 2019, Macao, China, August 10-16, 2019*, 1907–1913. ijcai.org.

Zhang, Y.; and Yan, J. 2023. Crossformer: Transformer Utilizing Cross-Dimension Dependency for Multivariate Time Series Forecasting. In *ICLR 2023, Kigali, Rwanda, May 1-5, 2023*. OpenReview.net.

Zhi, W.; Feng, D.; Tsai, W.-P.; Sterle, G.; Harpold, A.; Shen, C.; and Li, L. 2021. From hydrometeorology to river water quality: can a deep learning model predict dissolved oxygen at the continental scale? *Environmental science & technology*, 55(4): 2357–2368.